Evaluation of MegaVoltage Cone Beam CT image quality with an unmodified Elekta Precise Linac and EPID : A feasibility study.

Tim Markwell[2,1], Lakshal Perera[1] ,Jamie Trapp[1] , Andrew Fielding[1]

[1] School of Chemistry, Physics and Mechanical Engineering, Science and Engineering Faculty, Queensland University of Technology, Brisbane, Queensland, Australia

[2] Cancer Care Services, Royal Brisbane and Women's Hospital, Brisbane, Queensland, Australia

Author Contact Details: email: timmarkwell@gmail.com, Phone: 0421546866

Abstract

In order to increase the accuracy of patient positioning for complex radiotherapy treatments various 3D imaging techniques have been developed. MegaVoltage Cone Beam CT (MVCBCT) can utilise existing hardware to implement a 3D imaging modality to aid patient positioning. MVCBCT has been investigated using an unmodified Elekta Precise linac and iView amorphous silicon electronic portal imaging device (EPID). Two methods of delivery and acquisition have been investigated for imaging an anthropomorphic head phantom and quality assurance phantom. Phantom projections were successfully acquired and CT datasets reconstructed using both acquisition methods. Bone, tissue and air were clearly resolvable in both phantoms even with low dose (22 MU) scans. The feasibility of MegaVoltage Cone beam CT was investigated using a standard linac, amorphous silicon EPID and a combination of a free open source reconstruction toolkit as well as custom in-house software written in Matlab. The resultant image quality has been assessed and presented. Although bone, tissue and air were resolvable

in all scans, artifacts are present and scan doses are increased when compared with standard portal imaging. The feasibility of MVCBCT with unmodified Elekta Precise linac and EPID has been considered as well as the identification of possible areas for future development in artifact correction techniques to further improve image quality.

I. INTRODUCTION

With the increasing use of more complex radiotherapy planning and delivery such as Intensity Modulated Radiation Therapy[1] the need for accurate patient positioning at treatment time is vital for achieving improved treatment outcomes compared to conventional treatment schemes[2]. There are several methods currently used to determine patient setup accuracy using x-ray imaging to image the patient. Electronic Portal Imaging Device (EPID) images utilising the treatment beam are commonly used however it can be difficult trying to achieve a high level of positional accuracy due to the inherently low contrast images, and the lack of true 3D positional imaging [3]. KiloVoltage Cone Beam Computed Tomography (kVCBCT), using an additional kiloVoltage x-ray source and detector mounted inline or orthogonally to the treatment head is commonly used for a number of treatment regions[4,5,6,7,8]. kVCBCT uses the source and detector along with gantry rotation to acquire a volumetric image set of the patient.

kVCBCT provides good tissue and bone contrast[9,10] at a significantly lower dose, however it can be a significant added expense to the cost of a linac, and is susceptible to imaging artifacts due to metallic implants[11].

MegaVoltage Cone Beam CT (MVCBCT) is an alternative to these methods[12,13,14], using the current linear accelerator at no extra cost by using the treatment beam as the source, and

EPID as the detector for 3D imaging. Although acquired MVCBCT projections suffer from reduced contrast, effects from profile filtering and back projection as well as the slice based viewing can help improve resolvability of anatomy. It has the advantage of a reduced susceptibility to metallic induced artifacts[15,16] and can be used to acquire electron density distributions[17], which can later be used in dose calculations for adaptive therapies[15,18,19]. KVCBCT can also be used in a similar fashion for adaptive therapies[20,21]. A disadvantage of MVCBCT is the higher dose delivered per scan when compared to kVCBCT. However the dose can be reduced using careful optimization of the image acquisition and reconstruction methods[22,23] and can be managed in the planning stage with the treatment planning system model when planning the dose coverage of the therapy itself [24,25]. It should also be noted that the dose for kVCBCT imaging can also be reduced through protocol optimisation[26].

MVCBCT has been used clinically[15] with a number of studies investigating the quality of the images[22], the acquisition parameters[23] and Quality Assurance (QA) and control tests[27] for Siemens Oncor and Primus Linear accelerators (Siemens Oncology Care Systems, Concord, CA). These systems have pulse controlled readout of the EPID, and can use both the treatment beam and an optimised imaging mode using a low Z target[23,28] to acquire data. Another study investigated the modification of an Elekta Precise Linac with a low Z target[29] and feedback control mechanism for the radiation pulse and image readout while using a constant gantry angle and a turntable for phantom rotation[30]. Wave guide modifications to emit low energy electron beams have also been developed demonstrating improved image quality [31].

This current work investigates the feasibility of MVCBCT imaging using an unmodified Elekta Precise Linac, iView EPID and standard steel couch. Two delivery and acquisition methods are investigated to acquire MVCBCT images using the standard target, flattening filters and EPID readout software and triggering mechanisms. The aim was to assess the

image quality in the standard setup (minimal corrections applied) "as is" to investigate if MVCBCT was possible with this hardware and software configuration, as well as identify key areas where corrections can be developed to improve image quality. The necessity for this investigation arose from a potential clinical need due to the presence of IMRT capable linacs without 3D image guidance features and no provision for further hardware purchasing. As linacs are still available for purchase without kV imaging and older simpler therapy units are being recycled for use in developing countries[32,33] the possibility of a cheap 3D imaging modality with no extra hardware required can be beneficial for the accurate delivery of complex treatments in clinics with limited budgets.

II. MATERIALS AND METHODS

A. Delivery and Acquisition

A 6 MV photon beam from an Elekta Precise Linac and an iView GT EPID imaging system (Elekta AB, Stockholm, Sweden) was used to acquire projections of a Gammex phantom (Gammex 464®, Gammex RMI, Middleton, WI) [34] with a length of 16 cm and a diameter of 20 cm as well as an in house anthropomorphic head (approx. 15 cm x 20 cm x 24 cm) phantom using two methods of delivery as detailed below. Both phantoms were set-up isocentrically using the in room lasers and external markers.

A planning CT of the head phantom was acquired on a Toshiba Aquillion Large Bore CT simulator for reference.

1. Method one – Step and Shoot:

Method one utilized a step and shoot technique that involved manually incrementing the gantry angle for each projection. Images were acquired starting from 0 degrees, over 180 degrees of rotation (1 projection per degree) with 5 MU per projection, resulting in a total of 900 MU for the acquisition. Each projection was acquired using a 22.5 cm x 22.5 cm radiation field (defined at the isocentre) and an Elekta iViewGT EPID with 1024 x 1024 pixels at 16 bits/pixel. A flood image with no phantom present for each angle was also acquired to be used later in the processing and reconstruction stage. In this investigation for time efficiency a limited angular coverage (180 degrees vs 200 degrees) was used.

All images were acquired in this method using the clinical iView Software. The iView software performed averaging of 8 image frames at each projection angle, that is ~0.625 MU per frame or 5 MU per projection per degree. The iView software acquisition is triggered by the linac to avoid pulsing artifacts in the images.

2. Method two – Continuous delivery:

A scan was acquired using a continuously moving gantry over a 180 degree arc with a field size of 22.5 cm x 22.5 cm delivering 180 MU (approximately 1.1 MU/projection). A lower dose 22 MU scan (approximately 0.13 MU/projection) for the total arc was also acquired. A dose rate of 125 MU/min was used for the 180 MU scan, and a lower dose rate of 16 MU/min used for the 22 MU scan. EPID images were acquired at regularly spaced angles (approximately 1.1 degrees / projection), recording approximately 165 projections (no frame averaging) for the total arc. A panel readout time of approximately 540 ms was used with the default gain set in the software. A constant gantry speed was assumed and acquired images were distributed evenly from 0 to 180 degrees, although this assumption is not completely accurate due to acceleration of the gantry at the start and finish of the arc. Flood images were also acquired to be used later in the reconstruction stage. The time to acquire each scan was approximately 90 seconds.

Images were acquired using the XiS (Perkin Elmer) software which is installed on the clinical iView acquisition system. The software allowed the acquisition of continuous images and flexible file exporting. The version of the iView software that was used in method one would not allow the export of acquired movies, only single projections and therefore could not be used for continuous gantry acquisition. XiS software image acquisition was not triggered by the linac pulse, instead using a constant internal timer. Due to the low pulse repetition frequency (PRF) of the linac, an insufficient number of projections were acquired if the EPID readout was triggered by the linac pulse.

B. Projection processing

In method one, images are flood field and dark current corrected automatically by the iView software. Bad pixels were corrected using the bad pixel map created by the iView system. Median filtering (3x3) was applied using in-house code to reduce the noise and correct remaining dead pixels.

In method two, TIFF images were extracted from the XiS software format (.his) files using ImageJ (US National Institute of Health, Bethesda, MD). Flood field correction and median filtering was performed on the projections, using in house software written in MatLab (The MathWorks Inc,Natick, MA). For each matched phantom projection/flood projection some pulse artifact removal occurs during the flood division due to aligning of the pulse artifacts in the projections.

C. Reconstruction

Reconstruction of the acquired projections was performed using the open source package OSCaR (acronym : Open-Source Cone-beam CT reconstruction tool for imaging Research) [35] which is written in Matlab.

Reconstructions for method one (Step and Shoot) were performed using the Feldkamp Davis and Kress (FDK) algorithm[36]. A Hamming filter was used to filter the projections prior to back projection. A reconstruction volume of 401x401x481 voxels was used based on projections (512 x 512 pixels) with a pixel pitch of approximately 0.08 cm x 0.08 cm. Images from method one (Step and Shoot) were also reconstructed at the same resolution as method two (continuous) for comparison.

Method two used the same approach however 256 x 256 pixel projections with a pixel pitch of approximately 0.16 cm x 0.16 cm were used and reconstructed into a lower resolution volume of 241 x 241 x 241 voxels. As the scans for method two were lower dose, a volume with larger voxels was reconstructed to achieve an image with an improved contrast to noise ratio. Image pixel values were left unmodified after reconstruction and not converted to Hounsfield Units.

D. Image quality measurements

Image quality was assessed using the Gammex phantom for both methods. Metrics used by Morin et al. [22] and Gayou et al. [23] were measured to assess the images produced by the two methods.

1. Spatial Resolution

The spatial resolution was measured using the line pair module in the Gammex phantom. The module contains an arrangement of 15 mm x 15 mm regions each with a different number of line pairs per centimetre, ranging from 4 lp/cm to 12 lp/cm. The spatial resolution is determined by the highest lp/cm in which the individual light and dark bands can be distinguished.

2. Contrast to noise ratio

The contrast to noise ratio (CNR) was determined using equation (1) and by measuring the intensity of inserts in the CNR module of the Gammex phantom. Inserts of different materials were measured using a central region of interest (ROI_{insert}) and a surrounding ring shaped region of interest as the background ($ROI_{background}$). The insert materials were bone, air, acrylic and polyethylene going clockwise from the top right.

$$CNR = \frac{mean(ROI_{insert}) - mean(ROI_{background})}{1/2[stdev(ROI_{insert}) + stdev(ROI_{background})]} \quad (1)$$

CNR was measured in the head phantom for method two using regions of interest in tissue and bone, shown in Figure 1.

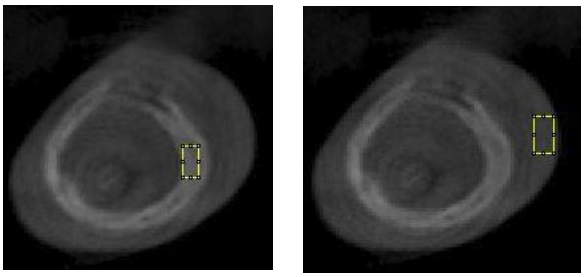

(a) (b)

Figure 1*: Slice from the head phantom at 180 MU showing the ROIs for bone (insert) in figure 1 (a) and tissue (background) figure 1 (b) used in method two.*

3. Uniformity

Uniformity was determined using equation (2) from Stützel[37] et al. by measuring regions of interest in the periphery, and centre of the uniformity module and calculating the difference shown in equation (2). Regions of interest for the measurements are shown in Figure 2.

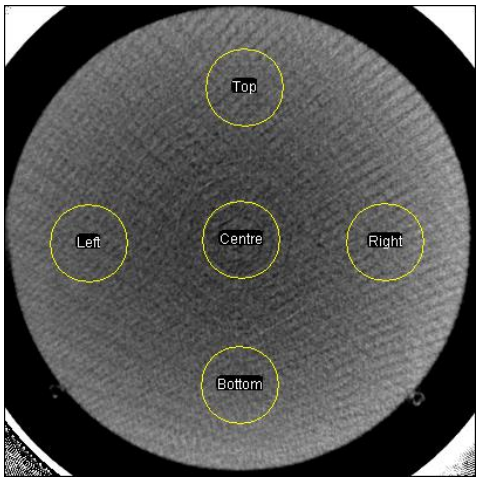

Figure 2: *Regions of interest used for uniformity measurements.*

$$Uniformity = \left| \overline{CT}_{peripheral\ ROI} - \overline{CT}_{centre\ ROI} \right| \quad (2)$$

E. Geometrical movement

Measurements of the movement of the EPID and gantry combination due to gravity were performed. A mechanical horizontal pointer on the couch was set to the isocentre by using a mechanical front pointer mounted on the collimator. Images of the horizontal pointer were acquired at each angle using a step and shoot approach in 10 degree increments over 180 degrees. A triangle was manually mapped to the tip of the pointer in each image, and the shift of the apex measured. This was a preliminary method used to determine the approximate

angle dependent movement in the gantry – panel system. This was performed for method one (Step and Shoot) and not measured for method two (continuous).

III. Results

Reconstructed images for method one (Step and Shoot) and method 2 (continuous) are presented below.

A. Spatial Resolution

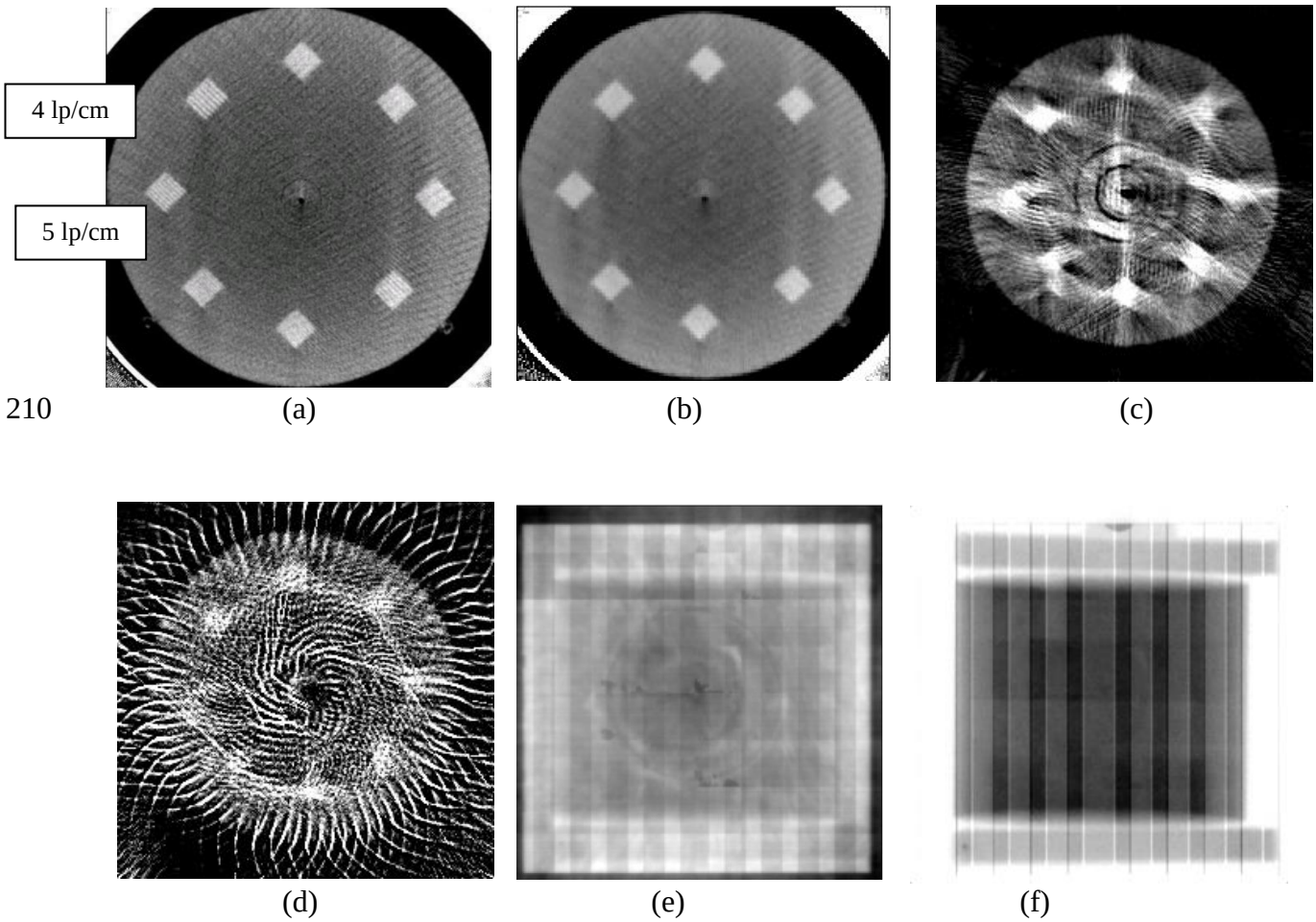

Figure 3 *: Line pair segment of the Gammex phantom. 5 lp/cm (9 o'clock position) and 4 lp/cm (11 o'clock position) were only resolvable for (a) method one (Step and Shoot) at a*

higher resolution and not (b) method one (Step and Shoot) lower resolution or c) method two (Continuous) 180 MU and (d) method two (Continuous) , 22 MU. (Note: Larger field of view shown in (c) and (d) to show artifacts). Figure 3(e) shows a projection of the Gammex phantom at 22 MU for method two (Continuous), (f) shows after flood correction (brightness and contrast adjusted to highlight phantom structure).The imaging window has been optimized for display of each image.

The 4 lp/cm section was clearly resolvable while the 5 lp/cm section was only just resolvable for method one in Figure 3(a) at the higher resolution. The spatial resolution sections in Figure 3(b), 3(c) and 3(d) show that the line pairs in the various sections are not resolvable. This is due to a combination of the lower reconstruction resolution shown by 3(b), and the lower image quality of projections acquired with method two (continuous) compared to method one (Step and Shoot). Figure 3 (d) also has a large pulse artefact pattern due to the continuous acquisition at a low pulse repetition frequency (PRF) , however the influence of pulse artifacts are less evident in Figure 3 (c) due to the increased dose and higher pulse repetition frequency. Glare artifacts possibly due to scatter in the detector and housing[38] as well as ring artifacts can also be seen in Figure 3(c).

Figures 3(e) shows a median filtered projection of the Gammex phantom for method two (continuous) at 22 MU. The effects of the low PRF can be seen by the large vertical stripes alternating in high and low intensity. These stripes move across the image in successive frames as the continuous acquisition is performed. Figure 3(f) shows the same projection after it has been flood corrected. The effects of the PRF artifacts are partially cancelled out resulting in thin vertical lines of high and low intensity, as compared to the large bands. The thin lines results from a slight phase mismatch between the flood projections and the phantom projections, which can change as the acquisition continues. This is due the slight variation in

linac pulsing at a low dose rate, as well as a small difference in the exact time the frames were acquired.

B. Contrast to Noise Ratio

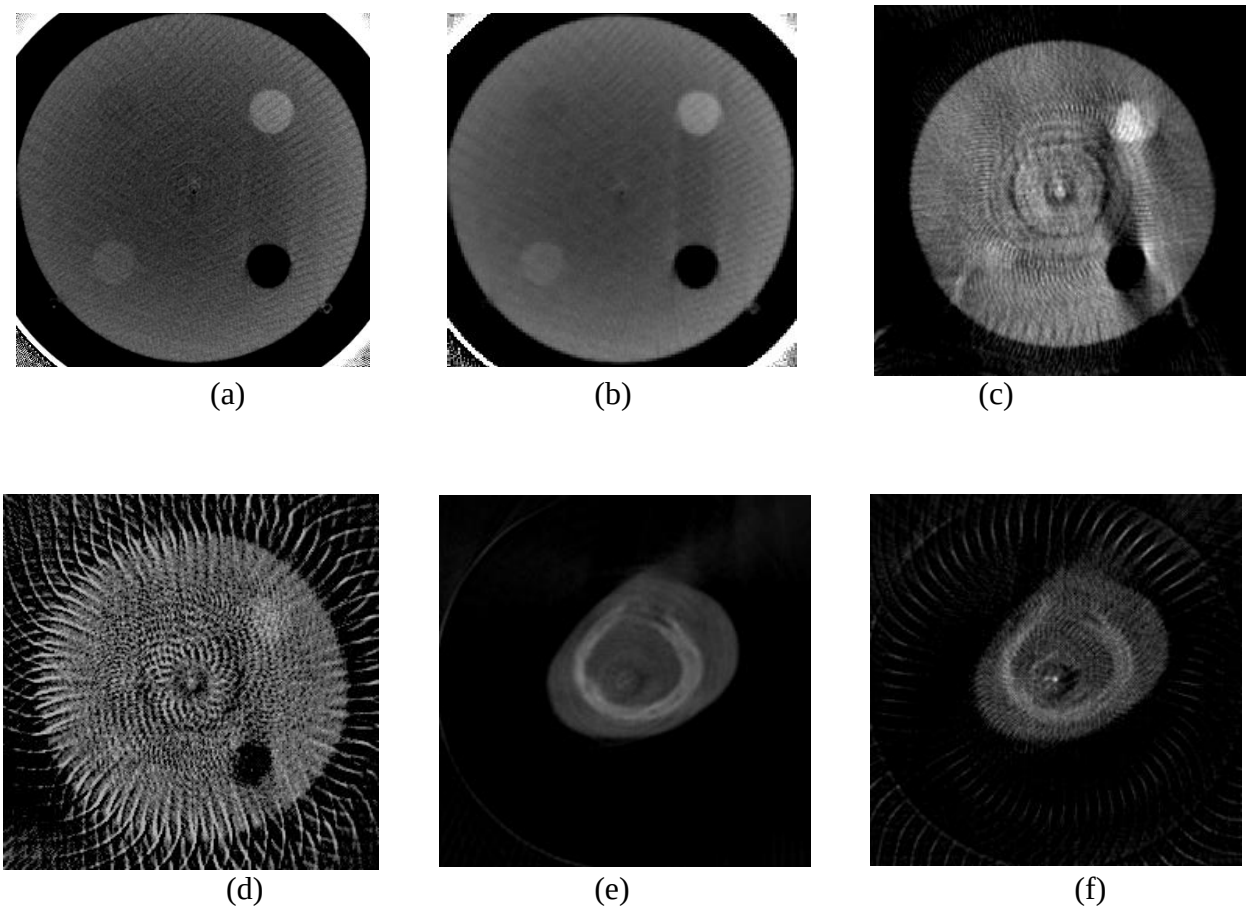

(a) (b) (c)

(d) (e) (f)

Figure 4 *: CNR module of the Gammex Phantom for method one (Step And Shoot) at the higher resolution (a) method one (Step and Shoot) at the lower resolution (b), method two*

(Continuous) 180 MU (c) and method two 22 MU (d). (e) and (f) show the section of the Head phantom used to measure CNR for method two 180 MU and 22 MU respectively.

The reconstructed slices used for CNR measurements from the insert section of the Gammex phantom for both methods are shown in Figures 4 (a)-(d) and the results of the CNR measurements are shown in Table I. The CNR measured in the head phantom for method two is shown in Figure 4 (e) and (f). The results for method one (Step and Shoot) are shown in Figures 4 (a) and (b), the four inserts can be clearly resolved, with bone (top right) and air (bottom right) having the greatest contrast. The results for method two, using a high dose (180 MU) can be seen in Figure 4 (c). Three of the four inserts are visible, with only a faint darkening in the area (top left) of the polyethylene insert. Image artifacts are present, with some shadow artifact cast by some inserts. Small pulse artifacts are also visible radiating from the centre of the image. Finally some ring artifacts are present due to some uncorrected bad pixels. The results of the 22 MU scan are shown in Figure 4 (d). Two of the inserts are visible with bone and air clearly shown. There are significant imaging artifacts present in the reconstruction resulting from pulse artifacts and the low signal-to-noise ratio due to the low dose of the scan. The shadow cast by the air insert is partially obscured by the other artifacts and the lower contrast of the reconstruction. As the primary purpose of this imaging modality is patient positioning, it can be seen that bone, air and soft tissue are visible in all scans.

Figures 4 (e) and (f) show the results from the head phantom for method two for 180 MU and 22 MU respectively. Tissue and bone in the head phantom are clearly resolvable for the low and high dose acquisitions. Figure 4(f) shows pulse artifacts due to the lower PRF for the 22 MU scan. The magnitude of this effect is less than those visible in the Gammex phantom and results from the better phase matching of the projection and flood image when the gain correction is performed. This has the effect of a significant cancelling out of the radiation pulse and readout artifacts in the projections prior to reconstruction. The degree of phase

matching between phantom sets (Gammex and head) compared with the flood projections varies slightly throughout the acquisition. Further, the increased scatter and attenuation of the larger Gammex phantom reduces the acquired signal which results in a decreased CNR. However, even with the presence of the imaging noise and artifacts, tissue and bone are clearly visible.

TABLE I**:** Contrast to noise ratio (CNR) of the Gammex phantom (a) and head phantom (b)

a)

Region	Method 1 (Step and Shoot) high resolution	Method 1 (Step and Shoot) low resolution	Method 2 (Continuous)(180 MU)	Method 2 (Continuous) (22 MU)
Bone	3.6	5.3	3.9	0.8
Air	10.6	13.6	3.4	2.6
Acrylic	1.2	2.1	0.3	0.1
Polyethylene	0.9	1.1	0.2	0.2

b)

Bone/Tissue	CNR
Head 22 MU	2.7
Head 180 MU	6.2

290

In Table I (a) the CNR is shown for each of the four inserts. In all results, air had the highest CNR followed by bone and acrylic. Polyethylene has a low CNR but is still visible. This correlates with the level of visibility of the inserts in Figure 4. The CNR decreases as the exposure of the scan decreases[37]. Again this is consistent with the greater visible noise in the
295 22 MU image and the presence of pulse artifacts. From the table it can be seen that method one (Step and Shoot) reconstructed at the lower resolution resulted in the highest CNR. This increase in CNR compared to the higher resolution reconstruction comes from the increased signal due to pixel binning prior to reconstruction.

Table I (b) lists the measured CNRs for 180 MU scan and 22 MU scans of the head phantom
300 using method two. The 180 MU scan had an improvement in CNR of approximately 2.3 when compared with the 22 MU scan. This change in CNR follows the recognised relationship of the CNR varying with the square root of dose.

C. Uniformity

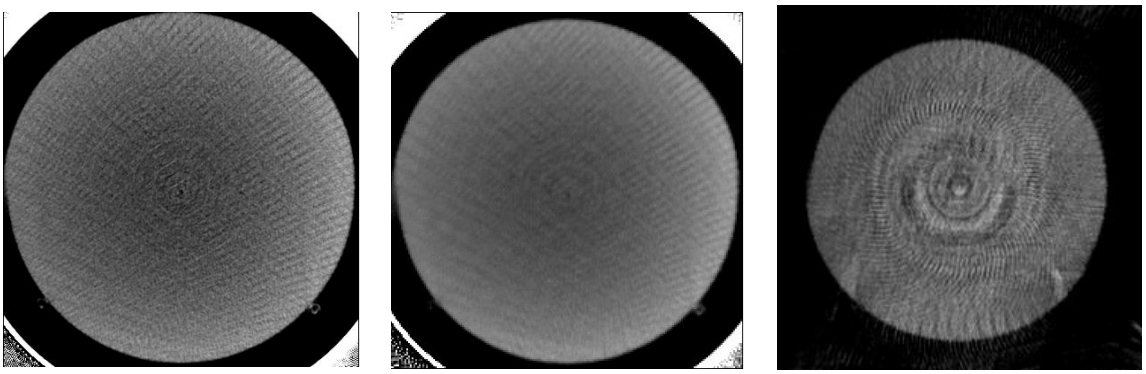

(a) (b) (c)

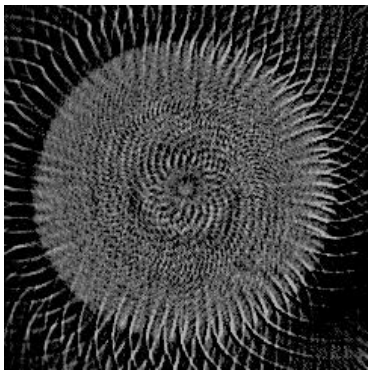

(d)

Figure 5:*Uniformity slices from the Gammex Phantom for (a) method one at a higher resolution (b) method one at the lower resolution (c) method two 180MU (d) and method two (22MU).*

Results from the uniformity measurements performed on the Gammex phantom are shown in Figure 5 and Table II. For method one shown in figure 5(a) and (b), a maximum uniformity variation of 27.8 pixel intensity units was determined. When expressed as the mean intensity of the right ROI when relative to the centre this is a variation of approximately 50% of the central ROI mean intensity value. The minimum uniformity variation was measured in the

left ROI. For method two shown by figures 5 (c) and (d), the 180 MU acquisition showed a significantly reduced uniformity variation in the left and top ROIs. For the 22 MU scan the minimum uniformity variation was measured in the right and top ROIs. The measurements of method two contain a larger variation due to the increased noise in the lower dose scans.

TABLE II : Uniformity of the various regions in the uniformity module of the Gammex phantom.

Region	Method 1 (Step and Shoot)	Standard Deviation	Method 1 (Step and Shoot) lower resolution	Standard Deviation	Method 2 (180 MU)	Standard Deviation	Method 2 (22 MU)	Standard Deviation
Centre	n/a	10.1	n/a	4.2	n/a	34.4	n/a	75.74
Left	13.5	8.05	14.2	4.8	1.5	24.48	33	74.24
Right	26.1	11.3	27.8	8.5	21.3	21.91	21.8	67.72
Top	20.2	9.6	19.7	6.5	6.3	26.41	24.3	72.57
Bottom	21.1	9.9	22.5	7.7	19.8	29.73	33.2	86.84

D. Mechanical movement

The change in X and Y coordinates of the apex of the triangle mapped to the horizontal pointer tip are shown in Figure 6. The pixels were measured then converted to distance using the pixel size of 0.39 mm/pixel.

A maximum variation of 2.34 mm in the Y direction was measured with a gantry angle between 140 and 180 degrees. A maximum variation of 0.78 mm in the X direction was also measured at gantry angles of approximately 140 to 180 degrees.

A summary is shown in Table III. There is a mean shift of -1.52 mm in the Y direction and a shift of -0.41 mm in the X direction.

TABLE III**:** Summary of difference in pointer position

	Y(mm)	X(mm)
Mean	-1.52	-0.41
Stdev	0.71	0.28
Max(mm)	-2.34	-0.78
Min(mm)	0	0

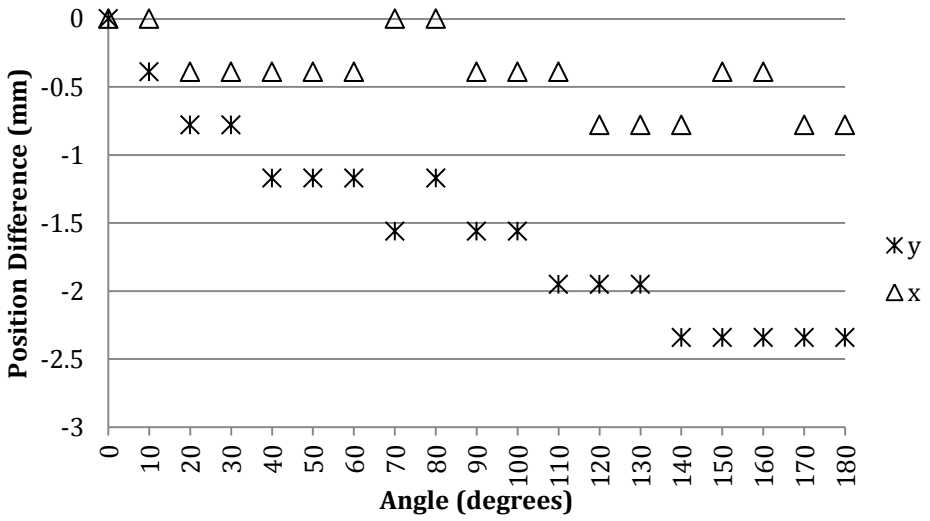

Figure 6: Graph of the difference in position of pointer tip versus the gantry angle in the x and y direction.

The measured gantry – panel movement manifests in the reconstruction as geometrically induced artifacts, such as small voids or small black areas in the centre of the images. Although this method uses a manual technique for measuring the tip position, it does

demonstrate some angular dependence of movement in the imaging acquisition. This is comparable with measurements performed in other studies[22,39].

F. Qualitative Assessment:

1. Method one:

Results from method one (Step and Shoot) are shown in Figure 7. In Figure 7(b) a volume render of the 3D reconstruction of the Gammex phantom is shown. The bone, air and acrylic inserts are clearly visible in the render. The metallic levelling screw used to adjust the phantom is also visible. From an overall perspective a clear likeness in shape and proportions exists when compared to the physical appearance of the actual phantom shown in Figure 7(a).

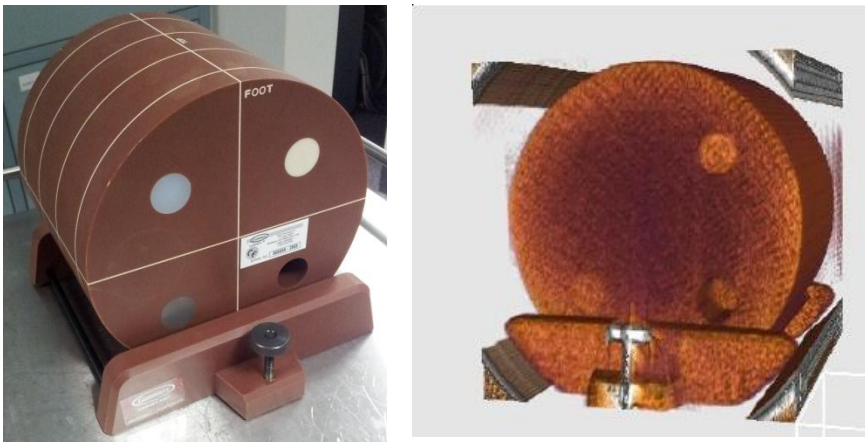

(a) (b)

***Figure 7** : Gammex Phantom (a), 3D Reconstruction (b) method one.*

2. Method two:

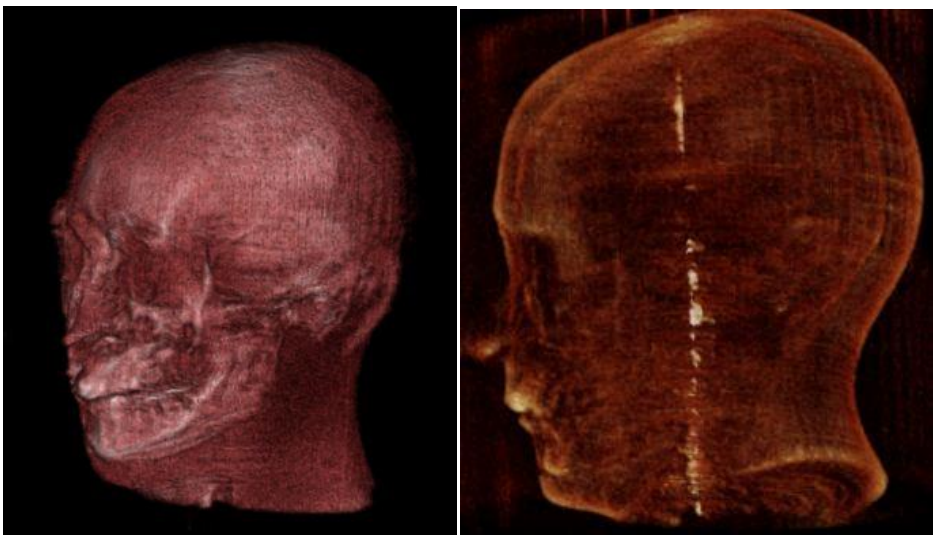

a) b)

Figure 8 *MIP Render a) Head phantom 180 MU, b) Head phantom 22 MU*

Figure 8 shows a MIP (Maximum Intensity Projection) render of the head phantom for the (a) 180 MU and (b) 22 MU scans. Bone and tissue are clearly identifiable in both images, with the 180 MU scan showing improved detail and contrast.

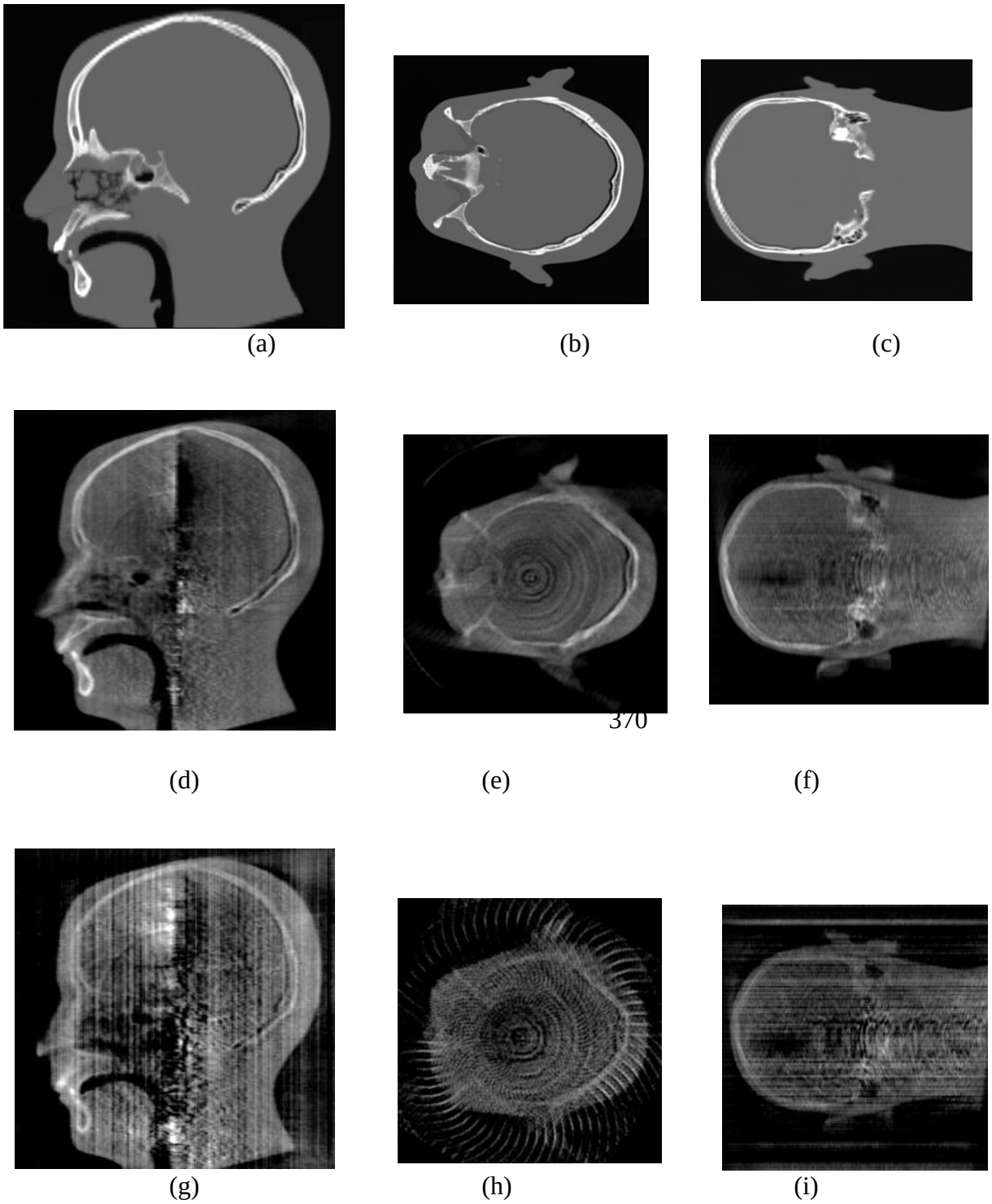

Figure 9*: View of the head phantom in the (a) and (d) sagittal (b) and (e) axial and (c) and (f) coronal directions 180MU ((d)-(f)) and 22MU ((g) – (i)). Image windows adjusted individually for display.*

Figure 9 shows sagittal, axial and coronal slices of the head phantom for the 180 MU and 22 MU scans. The axial image clearly reveals bone, tissue and hollow structures. Ring artifacts

are visible in (e) and (h), due to uncorrected pixels in the projections. In images (d) and (g) a large dark area can also be seen in the centre of the brain region, this is due to some geometrical movement, as well as artifacts acquired in the projections and the presence of cupping artefacts or non - uniformity in the images. In the 22 MU scan, bone and tissue as well as air cavities can be identified in the three views. Radiation pulse artifacts can be seen in the reconstructed images resulting in the vertical and horizontal stripes in figure 9 (g) and figure 9 (i) and the curved high intensity artifacts seen in figure 9 (h).

Various anatomical structures were resolvable in all MVCBCT images showing a reasonable reproduction compared with the planning CT images shown in figures 9(a-c).

IV. Discussion

In method one the very high dose (900 MU) and stationary gantry for each projection yielded reconstructed CT datasets with a high spatial resolution and good image quality. This method optimised gantry angle accuracy and allowed frame averaging and pulse triggering during projection acquisition, increasing the SNR and reconstruction image quality. This represents a possible image quality level "goal" to aim for in future investigations.

Method two yielded good results, with bone, tissue and air cavities being resolvable in all scans on the Gammex and anthropomorphic head phantoms at both dose levels. However the higher dose (180 MU) scans yielded improved results due to the increased exposure for the scan and increased PRF which reduced pulse artifacts. The 22 MU scans showed an increased noise due to the low exposure and reduction in image quality due to the significant pulse artifacts. The scan times were quite reasonable at both doses, with scans taking approximately 1.5 minutes.

In all axial images ring and pulse artifacts can be clearly seen. The concentric rings are due to bad pixels and under responding pixels in the EPID projections. Median filtering can reduce the noise however it is not completely effective at correcting all under responding pixels. Pulse artifacts are visible in all images acquired using method two due to the EPID being read out using an internal timer instead of being triggered by the trailing edge of the radiation ON pulse. In order to improve image quality without a gating system which can require linac modification and a possible increase in scan time depending on pulse rate and readout speed, custom image processing methods are being developed to correct for pulse artifacts in the projections prior to reconstruction. Results of this technique in development were not presented here due to the scope of the feasibility study and will form the subject of further work. Another group have also recently shown a possible method for correction[40] however this was not possible in our clinic due to operating restrictions.

In Figures 9 (d) and (g) there is a vertical artifact running down the centre of the phantom that is caused by the physical movement in the linac-EPID combination as well as other artefacts acquired in the original projections. Geometrical correction techniques have been developed previously[41,42] which could possibly be adapted to this system to however their application was outside the scope of this feasibility study.

Finally in Figure 9(e), an area is visible without a clearly defined boundary and some splaying artifacts (at approximately the 12 o'clock position in the figure) are visible. This is due to the incomplete angular sampling of the shorter scan arc (180 degrees vs 200 degrees). Some projections were missed due to the limited number of frames the EPID and XiS software combination could acquire due to buffer size, the speed at which the gantry could rotate and variability in angular distribution of acquired projections. Secondly, the manual start of image acquisition and the angle of the first exposed frame varied due to a variance in time to beam on, particularly at low dose rates.

The 22 MU scan of the head shows enough contrast to clearly distinguish bone, tissue and air cavities even in the presence of the artifacts mentioned previously. Although artifacts are present, the quality of images at 22 MU indicates future investigation into pre- and post-processing may be warranted. The quality of the volumetric data reconstructed suggests clinically useful images may be possible with appropriate artifact corrections at an exposure of approximately twice the current setup protocol of two 5 MU orthogonal images totalling 10 MU.

V. Conclusion

With the presence of an EPID the use of MegaVoltage Cone Beam CT on an unmodified Elekta Precise accelerator to aid the accurate setup of patients undergoing radiotherapy treatments has been shown to approach viable scan times and with further work offers a potentially useful clinical imaging modality. Using standard clinical linac hardware and a combination of a free open source reconstruction toolkit as well as custom in-house software written in Matlab a prototype MVCBCT system has been successfully implemented and assessed. Sources of artifacts influencing image quality have been identified as a target for further development to further increase the availability of MVCBCT as a 3D imaging modality.

ACKNOWLEDGMENTS:

This was partially funded by National Health and Medical Research Council grant 553012.

The authors like to thank Nigel Middlebrook for help acquiring data. We would also like to thank Scott Crowe, the High Performance Computing Centre, QUT, the Royal Brisbane and Women's Hospital and Elekta for their assistance.

References

[1] L.K. Mell, A.K. Mehrotra, and A.J. Mundt, "Intensity-modulated radiation therapy use in the U.S., 2004.," Cancer **104**(6), 1296–303, (2005).

[2] D. Jaffray, P. Kupelian, T. Djemil, and R.M. Macklis, "Review of image-guided radiation therapy.," Expert Rev. Anticancer Ther. **7**(1), 89–103, (2007).

[3] L.E. Antonuk, "Electronic portal imaging devices: a review and historical perspective of contemporary technologies and research," Phys. Med. Biol. **47**, R32–R65, (2002).

[4] J. Boda-Heggemann, F. Lohr, F. Wenz, M. Flentje, and M. Guckenberger, "kV cone-beam CT-based IGRT: a clinical review.," Strahlenther. Onkol. **187**(5), 284–91, (2011).

[5] N.A. Mc Parland, "kV-Cone Beam CT as an IGRT Tool in the Treatment of Early Stage Prostate Cancer: A Literature Review," J. Med. Imaging Radiat. Sci. **40**(1), 9–14, (2009).

[6] W.W.K. Fung and V.W.C. Wu, "Image-guided radiation therapy using computed tomography in radiotherapy," J. Radiother. Pract. **10**(02), 121–136, (2010).

[7] Z. Zumsteg *et al.*, "Image Guidance During Head-and-Neck Cancer Radiation Therapy: Analysis of Alignment Trends with In-Room Cone-Beam Computed Tomography Scans.," Int. J. Radiat. Oncol. Biol. Phys. **83**(2), 712–719, (2011).

[8] R.B. Den *et al.*, "Daily image guidance with cone-beam computed tomography for head-and-neck cancer intensity-modulated radiotherapy: a prospective study.," Int. J. Radiat. Oncol. Biol. Phys. **76**(5), 1353–9, (2010).

[9] A.R. Yeung *et al.*, "Tumor localization using cone-beam CT reduces setup margins in conventionally fractionated radiotherapy for lung tumors.," Int. J. Radiat. Oncol. Biol. Phys. **74**(4), 1100–7, (2009).

[10] M. Chan, J. Yang, Y. Song, C. Burman, P. Chan, and S. Li, "Evaluation of imaging performance of major image guidance systems.," Biomed. Imaging Interv. J. **7**(2), e11, (2011).

[11] Y. Zhang, L. Zhang, X.R. Zhu, A.K. Lee, M. Chambers, and L. Dong, "Reducing metal artifacts in cone-beam CT images by preprocessing projection data.," Int. J. Radiat. Oncol. Biol. Phys. **67**(3), 924–32, (2007).

[12] M. Broderick, G. Menezes, M. Leech, M. Coffey, and R. Appleyard, "A comparison of kilovoltage and megavoltage cone beam CT in radiotherapy," J. Radiother. Pract. **6**(03), 173–178, (2007).

[13] B.A. Groh, J.H. Siewerdsen, D.G. Drake, J.W. Wong, and D.A. Jaffray, "A performance comparison of flat-panel imager-based MV and kV cone-beam CT," Med. Phys. **29**(6), 967–975, (2002).

[14] O. Gayou and M. Miften, "Commissioning and clinical implementation of a mega-voltage cone beam CT system for treatment localization," Med. Phys. **34**(8), 3183, (2007).

[15] O. Morin *et al.*, "Megavoltage cone-beam CT: System description and clinical applications," Med. Dosim. **31**(1), 51–61, (2006).

[16] M. Meilinger, C. Schmidgunst, O. Schütz, and E.W. Lang, "Metal artifact reduction in cone beam computed tomography using forward projected reconstruction information.," Z. Med. Phys. **21**(3), 174–82, (2011).

[17] J. Chen, O. Morin, M. Aubin, M.K. Bucci, C.F. Chuang, and J. Pouliot, "Dose-guided radiation therapy with megavoltage cone-beam CT," Br. J. Radiol. **79**, S87–S98, (2006).

[18] O. Morin *et al.*, "Dose calculation using megavoltage cone-beam CT.," Int. J. Radiat. Oncol. Biol. Phys. **67**(4), 1201–10, (2007).

[19] A. Richter *et al.*, "Investigation of the usability of conebeam CT data sets for dose calculation," Radiat. Oncol. **3**, 13, (2008).

[20] J. Nijkamp *et al.*, "Adaptive radiotherapy for prostate cancer using kilovoltage cone-beam computed tomography: first clinical results.," Int. J. Radiat. Oncol. Biol. Phys. **70**(1), 75–82, (2008).

[21] G.X. Ding *et al.*, "A study on adaptive IMRT treatment planning using kV cone-beam CT.," Radiother. Oncol. **85**(1), 116–25, (2007).

[22] O. Morin *et al.*, "Physical performance and image optimization of megavoltage cone-beam CT," Med. Phys. **36**, 1421, (2009).

[23] O. Gayou, "Influence of acquisition parameters on MV-CBCT image quality," J. Appl. Clin. Med. Phys. **13**(1), 1–13, (2012).

[24] O. Morin, A. Gillis, M. Descovich, J. Chen, and M. Aubin, "Patient dose considerations for routine megavoltage cone-beam CT imaging," Med. Phys. (May), 1819–1827, (2007).

[25] A. Shah, E. Aird, and J. Shekhdar, "Contribution to normal tissue dose from concomitant radiation for two common kV-CBCT systems and one MVCT system used in radiotherapy.," Radiother. Oncol. **105**(1), 139–44, (2012).

[26] P. Ravindran, "Dose optimisation during imaging in radiotherapy," Biomed. Imaging Interv. J. **3(2)**(e23), (2007).

[27] A. Isambert, I.H. Ferreira, L.E. Nicula, G. Bonniaud, and D. Lefkopoulos, "Quality control of megavoltage cone beam CT imaging system," Cancer Radiother. **12**(8), 781–787, (2008).

[28] C. Beltran, R. Lukose, B. Gangadharan, a Bani-Hashemi, and B. a Faddegon, "Image quality & dosimetric property of an investigational imaging beam line MV-CBCT.," J. Appl. Clin. Med. Phys. **10**(3), 3023, (2009).

[29] D.A. Roberts, V.N. Hansen, A.C. Niven, M.G. Thompson, J. Seco, and P.M. Evans, "A low Z linac and flat panel imager: comparison with the conventional imaging approach.," Phys. Med. Biol. **53**(22), 6305–19, (2008).

[30] D.A. Roberts *et al.*, "Comparative study of a low-Z cone-beam computed tomography system.," Phys. Med. Biol. **56**(14), 4453–64, (2011).

[31] D.A. Roberts *et al.*, "Kilovoltage energy imaging with a radiotherapy linac with a continuously variable energy range," Med. Phys. **39**(3), 1218–1226, (2012).

[32] M.B. Barton, M. Frommer, and J. Shafiq, "Role of radiotherapy in cancer control in low-income and middle-income countries.," Lancet Oncol. **7**(7), 584–95, (2006).

[33] D. Odero and D. Shimm, "Third party EPID with IGRT capability retrofitted onto an existing medical linear accelerator," Biomed. Imaging Interv. J. (2009).

[34] Gammex Inc, *Gammex 464 Phantom*, http://www.gammex.com/n–portfolio/productpage.asp?, (n.d.).

[35] N. Rezvani, D. Aruliah, K. Jackson, D. Moseley, and J. Siewerdsen, "OSCaR: An open-source cone-beam CT reconstruction tool for imaging research," in (American Association of Physicists in Medicine, 2007), p. 2341.

[36] L.A. Feldkamp, L.C. Davis, and J.W. Kress, "Practical cone-beam algorithm," J. Opt. Soc. Am. A **1**(6), 612–619, (1984).

[37] J. Stützel, U. Oelfke, and S. Nill, "A quantitative image quality comparison of four different image guided radiotherapy devices.," Radiother. Oncol. **86**(1), 20–4, (2008).

[38] G. Poludniowski, P.M. Evans, a Kavanagh, and S. Webb, "Removal and effects of scatter-glare in cone-beam CT with an amorphous-silicon flat-panel detector.," Phys. Med. Biol. **56**(6), 1837–51, (2011).

[39] M.A. Mosleh-Shirazi, P.M. Evans, W. Swindell, S. Webb, and M. Partridge, "A cone-beam megavoltage CT scanner for treatment verification in conformal radiotherapy," Radiother. Oncol. **48**(3), 319–328, (1998).

[40] M. Mooslechner, B. Mitterlechner, H. Weichenberger, S. Huber, F. Sedlmayer, and H. Deutschmann, "Analysis of a free-running synchronization artifact correction for MV-imaging with aSi:H flat panels," Med. Phys. **40**(3), 031906, (2013).

[41] Y. Cho, D.J. Moseley, J.H. Siewerdsen, and D.A. Jaffray, "Accurate technique for complete geometric calibration of cone-beam computed tomography systems," Med. Phys. **32**, 968, (2005).

[42] J. Pouliot *et al.*, "Low-dose megavoltage cone-beam CT for radiation therapy," Int. J. Radiat. Oncol. **61**(2), 552–560, (2005).